

Extracellular Vesicle Production Loaded with Nanoparticles and Drugs in a Trade-off between Loading, Yield and Purity: Towards a Personalized Drug Delivery System

Max Piffoux, Amanda K. A. Silva,* Jean-Baptiste Lugagne, Pascal Hersen, Claire Wilhelm, and Florence Gazeau*

Extracellular vesicles (EVs) released by cells and circulating in body fluids are recognized as potent vectors of intercellular self-communication. Due to their cellular origin, EVs hold promise as naturally targeted “personalized” drug delivery system insofar as they can be engineered with drugs or theranostic nanoparticles. However, technical hurdles related to their production, drug loading, purification, and characterization restrain the translation of self-derived EVs into a clinical drug delivery system. Herein, different methods are compared to generate and to purify EVs encapsulating iron oxide nanoparticles and a clinical photosensitizer drug (Foscan) as biocomouflaged agents for photodynamic therapy, magnetic resonance imaging, magnetic manipulation, and hyperthermia. Theranostic EVs are produced from drug- and nanoparticle-loaded endothelial cells either by spontaneous release in complete medium, by starvation in serum-free medium or by mechanical stress in a microfluidic chip mimicking vessel shear stress, and purified by ultracentrifugation or magnetic sorting. The impact of the production and purification protocols is investigated on EV yield and size, nanoparticle and drug cargo, and finally on their therapeutic efficacy. EV production by starvation combined with purification by ultracentrifugation may be considered a reasonable trade-off between loading, yield, and purity for biogeneration of theranostic EVs.

1. Introduction

Specific delivery of nanoparticles and drugs to target sites of diseases is one of the most popular grail in nanomedicine. However, drug delivery systems (DDS) face physical and biological barriers in the body that limit their access to the target tissue.^[1] In the aim to develop personalized medicine, multivalent targeting agents fitting the molecular profile of the patient are expected to enhance the delivery efficiency of chemically derived DDS. Nevertheless, the development of personalized

vectors adapted to each patient brings along economical as well as technical hurdles that restrict clinical translation. An ultimate strategy toward personalized medicine is the use of biological material from the patient, leveraging its inherent adaptation to the actual molecular state of the individual and of the pathology. In this direction, DDS consisting of the patient cells or of cell byproducts hold promise as a future generation of biocomouflaged vectors with longer circulation time, enhanced capacity to cross biological and physical barriers, and natural targeting properties.^[2] For example, macrophages and mesenchymal stem cells have been used as nanoparticle transporters with remarkable tumor homing properties.^[3] More minimal system consists of nanoparticles encapsulated into cellular membrane ghost after cell disruption.^[4] These ghosts recapitulate some of the cell properties and dramatically change the biodistribution of nanoparticles.^[5]

However, the human body possess its own outperforming delivery device in extracellular vesicles (EVs), which are released by cells in a constitutive manner or in response to stress and circulate in all body fluids.^[6] Indeed EVs act as a far-reaching intercellular communication pathway controlling cell signaling, due to their unique capability to transport and transfer membrane proteins and lipids as well as RNA and cytoplasm components from parental cells to distal cells.^[7,8] By conveying biological informations, EVs are active effectors in the regulation of physiological processes, such as coagulation,^[9] immune response,^[10] pregnancy^[11] as well as pathologic ones related to infection,^[12] and cancer.^[13]

In addition to their intrinsic roles, EVs may be engineered to harbor exogenous therapeutic or theranostic payload.^[14] In this strategy, the aim is to translate such cell communication effectors into an intrinsically biocompatible and personalized delivery system. Indeed, as conveyors of biological cargoes, EVs feature advantageous attributes of delivery vehicles: they harbor adapted lipid and protein composition, size, and flexibility that enable them to travel across biological membranes and target specific cells.^[15] Additionally, EVs shelter their internal cargo, such as proteins and genomic material, from the harsh

M. Piffoux, Dr. A. K. A. Silva, Dr. J.-B. Lugagne,
Dr. P. Hersen, Dr. C. Wilhelm, Dr. F. Gazeau
Laboratoire Matière et Systèmes Complexes
UMR 7057
CNRS and Université Paris Diderot
10 rue Alice Domon et Léonie Duquet, 75205 Paris Cedex 13, France
E-mail: amanda.silva@univ-paris-diderot.fr;
florence.gazeau@univ-paris-diderot.fr

DOI: 10.1002/adbi.201700044

extracellular environment space. The possibility of customizing EVs from patient cells with exogenous imaging tracers and therapeutic drugs, nanoparticles or nucleic acids opens up a wide range of therapeutic perspectives. However, the use of EVs as personalized DDS brings along technological challenges related to their production, loading,^[16] purification, and characterization. EVs are spontaneously produced during cell culture or released in response to a biological, chemical, or physical trigger. EV release in complete culture medium^[17] or in response to serum or oxygen deprivation is the most common EV production methods, mimicking the stressful conditions of tumor microenvironment and injured tissues. Because endothelial cells undergoing shear stress in vessels are a major source of blood-circulating EVs, recent production approaches also rely on mechanical methods in which precursor cells undergo shear stress via extrusion,^[18] microfluidic devices,^[19] or sequential filtration.^[20] Although there are several methods for EV production, the lack of comparison between them and inconclusive EV characterization data make it difficult to point out which approach is the most suited for theranostic applications and clinical translation.

Apart from production, the isolation of EVs also represents a challenging issue considering the subcellular size range and confounding effects related to protein aggregate contamination. Ultracentrifugation (UC) is the most common method to isolate EVs. A major hurdle of using ultracentrifugation-based purification methods is the impact of G force on vesicles. The acceleration force may lead EVs to fragment, leak their cargo, or become activated. Besides, centrifugal acceleration of 100 000 to 200 000 g may induce vesicle fusion and protein sedimentation.^[21] All these effects may influence EV properties and purity. Therefore, other methods have been investigated for EV isolation such as ultrafiltration,^[22] immunoaffinity capture,^[23] size exclusion chromatography,^[24] or magnetic sorting (for EVs labeled with magnetic nanoparticles).^[25]

Considering the multiple options to produce and purify EVs, the best choice is unclear and comparative studies are needed. Of note, comparative studies should be supported by in-depth EV characterization by multiple technique analysis. Indeed, no single analysis method may provide thorough EV characterization.^[26] Techniques must be combined systematically in the attempt to perform an EV characterization as complete as possible.

We have shown in a previous study that cells labeled with both magnetic nanoparticles and a clinical photosensitizer drug (meta-tetrahydroxyphenylchlorin—mTHPC, commercialized under the brand name Foscan) could release EVs incorporating together iron oxide nanoparticle and drug cargoes. These hybrid EVs—called theranosomes—represent a biocompatible delivery system for cancer theranostics, combining magnetic resonance imaging (MRI) and fluorescent detectability and on demand activation by laser irradiation to induce photodynamic therapy as demonstrated *in vitro* and *in vivo*.^[25] Additionally, iron oxide nanoparticles confer magnetic properties to EVs which can be manipulated and sorted by magnetic forces. However potential clinical translation requires optimization of production and isolation with concomitant in depth characterization of theranosomes. Herein, we present a microfluidic method for rapid triggering of EV release by endothelial

cells and we compared such instant mechanical stress to conventional 3 d starvation stress or spontaneous release in complete medium. The impact of the different production protocols on precursor cells and offspring vesicles was investigated by imaging flow cytometry (ImageStream^X (IS^X)), a high throughput method to characterize cells, debris, and EVs. We compared two isolation protocols to purify EVs: ultracentrifugation and magnetic sorting. Nanoparticle tracking analysis (NTA), protein dosage characterization techniques were then combined to IS^X in order to access the yield and purity as well as to evaluate size and loading features of the EVs obtained by the different production and purification methods. Finally, we tested the phototoxicity of these drug-loaded EVs on cancer cells. The purpose of the study is to establish a benchmark for a rational choice of production and purification methods to generate theranostic self-derived EVs.

2. Results and Discussion

In order to produce multifunctional EVs loaded with superparamagnetic nanoparticles (PM) and mTHPC photosensitizer drug (PTS), human umbilical vein endothelial cell (HUVEC) endothelial cells were incubated with both PM and PTS (PMPTS cells) or with PM or PTS separately, previous to EV production (Figure 1a). Considering mechanical methods as emergent approaches for rapid EV production,^[18–20] we investigated a microfluidic biomimetic method for EV generation. The approach is inspired by EV release in response to shear stress in vessels and capillaries accounting for natural EVs generation in the organism. We designed a microfluidic device consisting of 200 parallel microchannels to induce mechanical shear stress on cells. The forced passage of cells into 10 μm thick, 5 μm wide, and 500 μm long microchannels at high speed (about 16 cm s⁻¹) (chip condition, Figure 1b–d) leads to membrane budding and EV release. Cell passage through microchannels could be monitored by time-lapse videomicroscopy as illustrated in Figure S1 (Supporting Information). Cells, debris, and EVs were recovered at the channels' outlets. For the sake of comparison, EVs were also produced by two established methods: 3 d culture in serum-free culture medium (starvation condition) and 3 d culture in culture medium supplemented with exosome-depleted serum (serum condition) (Figure 1).

2.1. EV Production Methods Differently Affect the Viability of Precursor Cells and Their Release of Nanoparticles and Drug

Because cell stress dramatically influences EV generation and properties, we first compare the impact of the different production methods on the precursor cell viability, area, circularity, PM and PTS content, and debris formation. This multiparameter investigation was conducted by imaging flow cytometry (IS^X) which combines high throughput analysis in flow stream and high resolution multispectral imaging.^[27] IS^X was used to analyze simultaneously both the parent cells and offspring apoptotic bodies or debris, before and after physical or starvation stress.

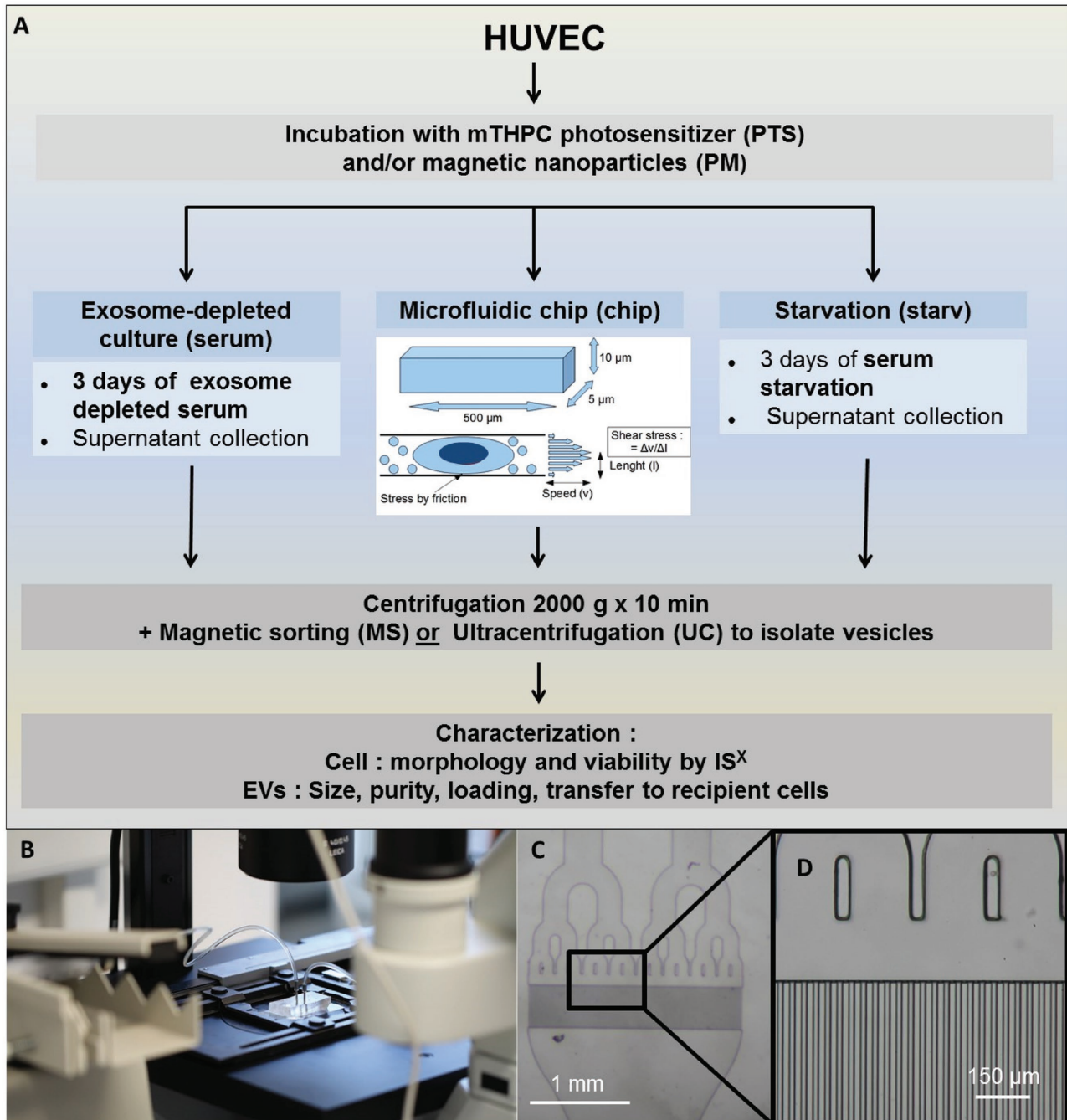


Figure 1. Investigation of EV production and purification methods. A) Schematic workflow of EV production and purification method as well as the characterization techniques performed. B) Bioinspired mechanical microfluidic method for EV production based on the effect of cell friction against vessel walls accounting for natural release process of EVs in blood capillaries. C) Macroscopic view of microfluidic chip for EV production. D) Microscopic view of microfluidic chip for EV production featuring 200 parallel microchannels (5–10 μm wide and 500 μm long).

Figure 2 displays representative images of cells (Figure 2A) and debris (Figure 2B) which were selected according to their areas (Figure S2, Supporting Information). Blebs can be observed on parent cells as well as vesicle budding, a feature quantified by the measure of cell circularity (Figure 2C). Additionally, the release of EVs and debris has been objectivized by loss of cell area (Figure 2D). Cell labeling with PM by itself resulted in a fivefold increase of debris (Figure 2F)

and a significant reduction in cell area compared to untreated control cells (Figure 2D). However, this PM-induced stress could be reversed by cell culture in nutritive medium, which decreased the percentage of debris compared to the starting PMPTS cells. Cell loading with PTS alone induced no effect in cell area or in the percentage of debris.

The culture in exosome-depleted complete medium had no impact on cell viability, whereas starvation and mechanical

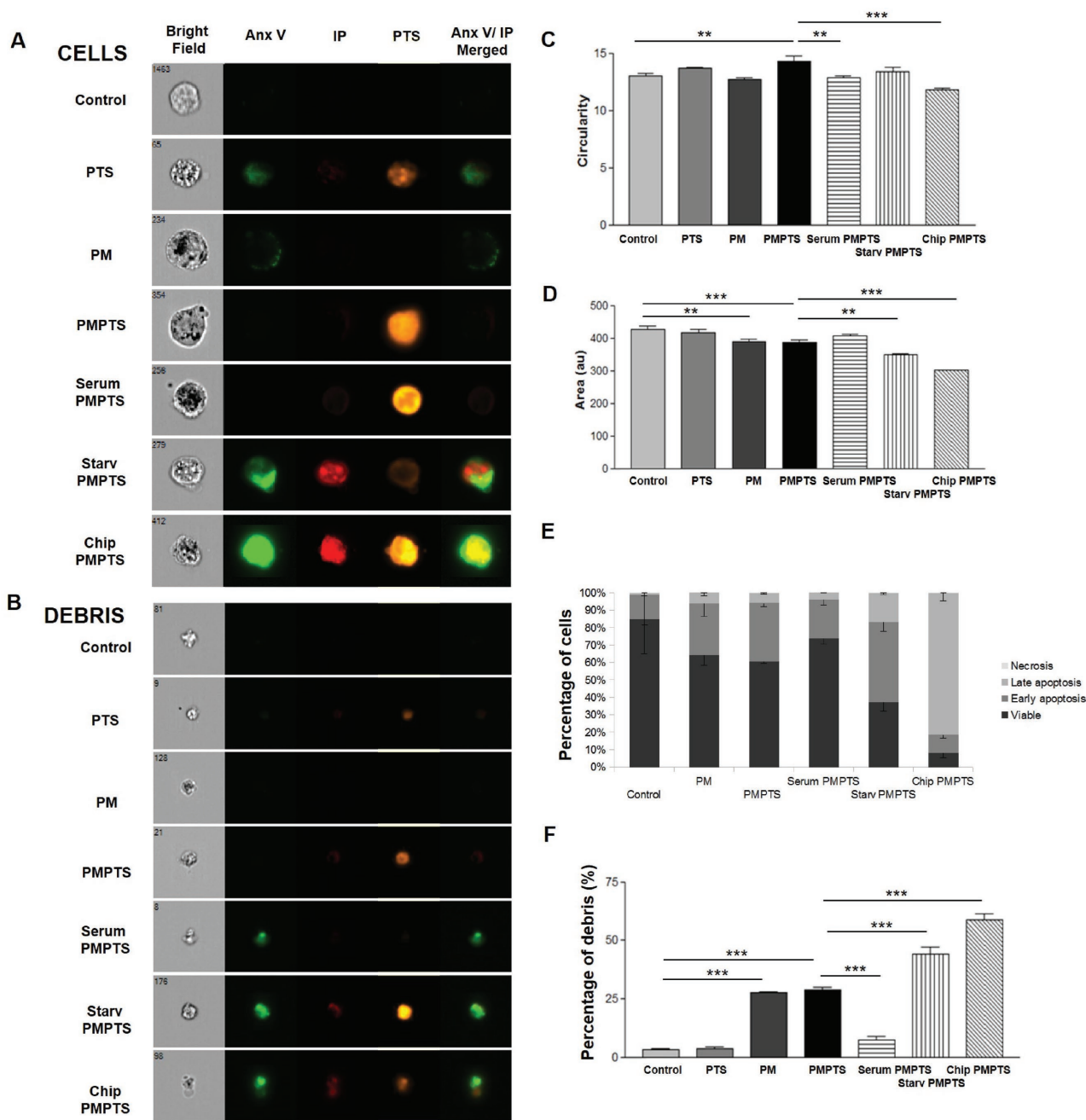


Figure 2. Impact of vesicle production methods on precursor cells and debris by ISX. Representative images of A) HUVEC and B) their debris following loading with magnetic nanoparticles (PM) and photosensitizer (PMPTS), culture in exosome-depleted complete medium (Serum), culture under serum-free starvation (Starv) or mechanical stress via the microfluidic chip (Chip). Control represents untreated cells and debris. Images were acquired in four different channels (bright field, Anaxin–fluorescein isothiocyanate (FITC) green fluorescence, iodide propidium (IP) red fluorescence, mTHPC orange fluorescence). The last column is the overlay FITC/propidium iodide. C) Cell circularity and D) cell area analyzed using IDEAS software based on bright field cell pictures. E) Percentage of cells distributed in either viable (AnxV–/IP–), early apoptotic (AnxV+/IP–), late apoptotic (AnxV+/IP+), or necrotic (AnxV–/IP+). F) Percentage of debris among the whole number of detected events (cells + debris). *, **, and *** indicate $P < 0.05$, $P < 0.01$, and $P < 0.001$, respectively, versus control (for PM, PTS, and PMTS) or versus PMPTS (for Serum PMPTS, Starv PMPTS, and Chip PMPTS).

stress reduced the viability of double-labeled PMPTS cells by a factor 2 and 6, respectively (Figure 2E). About half of the cell population was in early apoptosis following starvation while mechanical stress induced the massive late apoptosis (about 80% of the cell population). Consistently, mechanical stress

induced the highest impact on the cell circularity, which reflects the occurrence of cell protrusions and blebs characteristic of apoptotic cells (Figure 2C). The reduced cell circularity following mechanical stress probably result from cell deformation during their passage through microfluidic tiny channels.

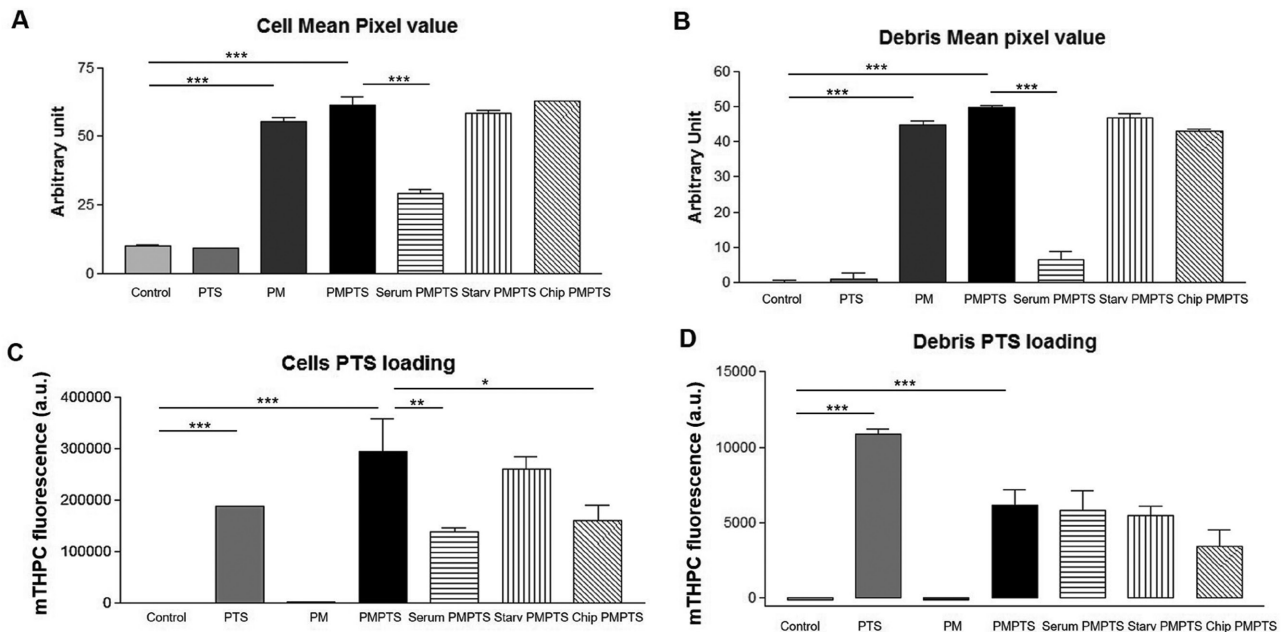


Figure 3. Evaluating the transfer of magnetic nanoparticles and photosensitizer from cells to debris by IS^X. Absolute mean pixel value in bright field images is indicative of PM loading for A) cells and B) debris as a function of cell treatment: loading with magnetic nanoparticles (PM), loading with magnetic nanoparticles and mTHPC photosensitizer (PMPTS), culture in exosome-depleted complete medium (Serum), culture under serum-free starvation (Starv), or mechanical stress via the microfluidic chip (Chip). PTS fluorescence emission by C) precursor cells or D) cell debris as a function of cell treatment. *, **, and *** indicate $P < 0.05$, $P < 0.01$, and $P < 0.001$, respectively, versus control (for PM, PTS, and PMPTS) or versus PMPTS (for Serum PMPTS, Starv PMPTS, and Chip PMPTS).

Mechanical stress and, in a lesser extent, starvation stress also reduced the cell area. This effect could be correlated to a loss of cellular material, which may be indicative of EVs and debris release. Indeed, the percentage of debris shifted from 30% for starting PMPTS cells to almost 50% and 70% following starvation and mechanical stress, respectively (Figure 2F). Cell debris may be regarded as an important parameter as they represent the highest size fraction of EV population comprising apoptotic bodies and microvesicles (MVs).

IS^X was also used to investigate cell loading with PM and PTS and the transfer of this dual cargo to cell debris. PM loading was determined via the absolute value of mean pixel signal on IS^X bright-field images which proved before to be a reliable indicator of intracellular nanoparticle concentration.^[28] Indeed, mean pixel values increased by a factor of 5 for PM-loaded cells compared to control and PTS-loaded cells (Figure 3A). Following starvation or mechanical stress in the chip, PM-loaded cells displayed equivalent mean pixel values. However, mean pixel values decreased by a factor two for cells cultured in exosome-depleted complete medium, probably due to cell division and PM dilution. The mean pixel values were highly correlated for cells and debris ($R^2 = 0.94$) (Figure 3A,B), the higher the PM loading of precursor cells, the higher the PM loading for the released debris.

PM loading in debris was also evaluated by the percentage of debris above a mean pixel value threshold (Figure S3, Supporting Information). PM loading was observed for about 80% of debris from PM-labeled cells and following starvation or mechanical stress. In contrast, the percentage of PM-loaded debris was only 10% in exosome-depleted complete culture medium in agreement with mean pixel value data.

PTS loading was investigated by mTHPC fluorescence emission in cells and debris (Figure 3C,D). Of note, culture in exosome-depleted complete medium as well as starvation and mechanical stress reduced the fluorescence emission of PMPTS cells, but this effect was more important in complete medium probably owing to cell division. As observed for PM, PTS load in debris correlated to PTS load in parent cells confirming a transfer of the drug in debris ($R^2 = 0.38$) (Figure 3C,D).

Overall, the chip-induced mechanical stress had the highest impact on cell viability, shape, and size, accompanied by debris formation. In comparison, 3 day-starvation in serum free medium has a weaker effect on precursor cells, while cell culture in exosome-depleted complete medium can be regarded as a mild and even restorative method. In fact, the magnetic nanoparticles and to a lesser extent the photosensitizer by itself decreased viability and enhanced debris formation. Culture in exosome-depleted complete medium counteracted this effect probably due to (i) cell proliferation and consequent cargo reduction via its repartition between daughter cells, (ii) reversion of early apoptotic state, and (iii) recapture of cell debris reaching an equilibrium state between emitted and reinternalized EVs.^[29]

2.2. Correlating EV Number and Purity with Different Methods Avoids Misleads When Comparing Production and Purification Methods

The conditioned medium of cells recovered from the microfluidic outlet and cultured in serum-free or exosome-depleted

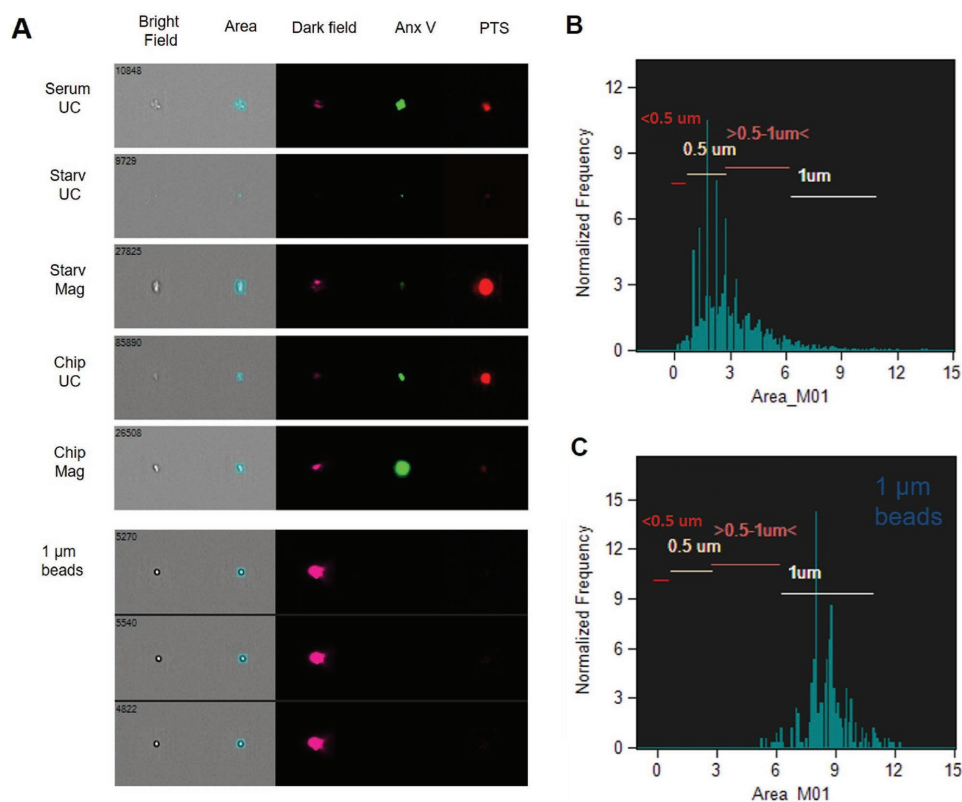


Figure 4. EV detection by IS^X. A) Representative images from IS^X of EVs and 1 μm calibration beads. EVs were obtained from HUVEC cells following loading with magnetic nanoparticles and mTHPC photosensitizer (PMPTS), culture in exosome-depleted complete medium (Serum), culture under serum-free starvation (Starv), or mechanical stress via the microfluidic chip (Chip) followed by either ultracentrifugation as a purification process (UC) or magnetic sorting (Mag). Images were acquired in four different channels (bright field, dark field, annexin-FITC green fluorescence, mTHPC (PTS) red fluorescence). The second column shows the mask generated by IDEAS software to assess area. Histograms represent area distribution for B) EVs from Starv UC condition and C) 1 μm beads.

complete medium, was centrifuged to remove dead cells and apoptotic bodies (2000 g for 10 min). In order to isolate EVs from the obtained supernatant, we compared two purification techniques: ultracentrifugation, the first-choice conventional method for EV isolation, and magnetic sorting. This alternative strategy is based on magnetic attraction of EVs labeled with PM. Magnetic sorting was proved cost effective for cell sorting and its implementation for single step EV purification could replace the centrifugal force.

The protocol of ultracentrifugation was designed to retrieve both the exosomes and microvesicles from serum, starvation, and chip supernatant (UC condition: 100 000 g for 1 h) or to pellet only the exosome fraction (UC exo: 10 000 g for 20 min, followed by 100 000 g for 1 h).

The characterization of single EVs by IS^X has been reported, overcoming the capabilities of conventional flow cytometry.^[30] IS^X was used here for the first time to analyze EV yield, size, and purity as well as dual nanoparticle and PTS cargo depending on the production method and purification protocol. While IS^X analysis of cell and debris was made using a $\times 40$ objective, the use of $\times 60$ objective makes it amenable to EV detection and analysis. EVs were labeled with Annexin V to assess phosphatidylserine exposure on EV outer membrane. **Figure 4A** displays some representative IS^X images when no threshold was settled

for detection, showing EVs and internal calibration beads of 1 μm diameter as an example. We could separate populations of objects that were single positive for Annexin V or for PTS, double positive or double negative (Figure S4, Supporting Information). Internal beads were easily distinguished from EVs due to their much larger dark field intensity and served to calibrate and quantify the total number of objects per mL. Nanoparticle load in EVs was evaluated via dark field intensity, as we have previously reported that nanoparticles enhance dark field intensity due to their light scattering properties.^[28] Relative sizing of EVs could be performed on focused events in comparison to calibrated multifluorescent 0.5 μm beads and to internal 1 μm beads as illustrated in Figure 4B,C and Figure S4 (Supporting Information).

The EV yield obtained by the different production/purification protocols was analyzed comparatively via NTA and IS^X on the basis of the total number of objects detected by each technique (**Figure 5**). NTA counts were higher than IS^X by three to four orders of magnitude (Figure 5A,B) because NTA features a detection threshold in size which is much smaller than IS^X and detects particles in general, including EVs as well as protein aggregates.^[31] In contrast IS^X could classify objects with respect to their fluorescence intensities (Anx5-FITC and mTHPC) and relative sizes.

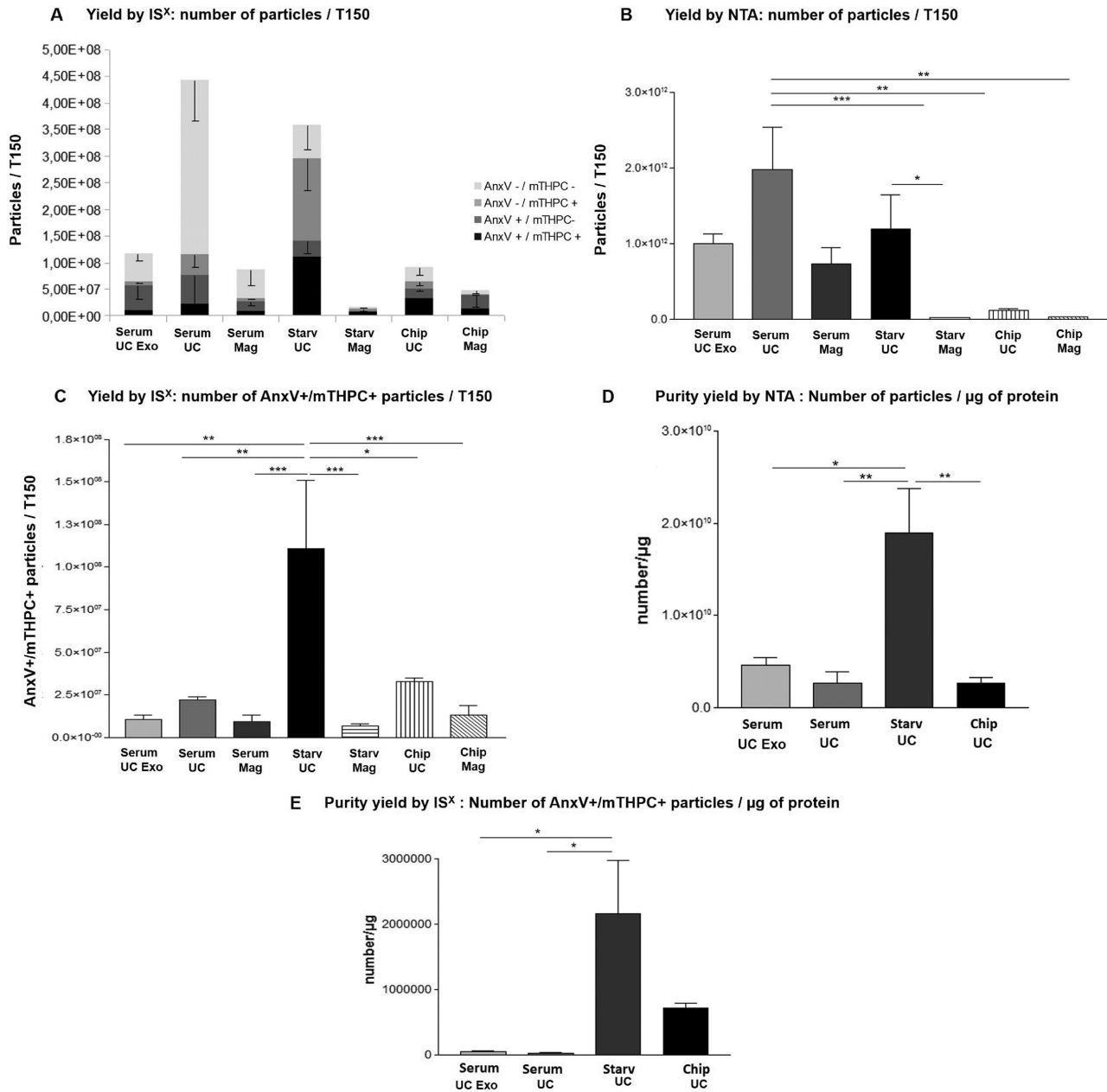


Figure 5. Vesicle yield and purity from the different production and purification methods by NTA and IS^X. Enumeration of HUVEC vesicle yield by A) IS^X and B) NTA and of double mTHPC and AnxV positive EV yield by IS^X for the different production and purification methods: culture in exosome-depleted complete medium (serum), culture under serum-free starvation (starv), or mechanical stress via the microfluidic chip (chip), purification being performed by ultracentrifugation (UC) or magnetic sorting (MAG). C) Enumeration of HUVEC double mTHPC and AnxV positive vesicle yield by IS^X. D) Vesicle purity assessed via the ratio of NTA particle count to protein mass by Bradford assay and E) Vesicle purity assessed via the ratio of double mTHPC and AnxV positive EVs events to protein mass by Bradford assay as a function of the production and the purification methods. *, **, and *** indicate $P < 0.05$, $P < 0.01$, and $P < 0.001$.

NTA indicated that particle yield by spontaneous release in complete medium (serum UC) was superior to starvation condition, which in turn, was superior compared to chip production (Figure 5B). IS^X displayed a similar trend when evaluating the totality of detected objects (i.e., single positive to annexin V or mTHPC, double positive and double negative) comprising also protein aggregates (Figure 5A). According to both NTA

and IS^X, the fraction expected to comprise both exosomes and microvesicles (serum UC) was more numerous than the fraction containing only exosome (serum UC exo). Both techniques also indicate that magnetic sorting was less efficient than ultracentrifugation to isolate EVs.

Interestingly, IS^X indicated that starvation UC condition displayed the highest yield when considering only the

double positive objects (Figure 5C), which indicates that it was more appropriate than serum UC condition to produce PTS-loaded phosphatidylserine-exposing EVs. Conversely, the highest fraction of double negative objects (about 50%) was observed for serum UC compared to less than 20% and 30% for starvation UC and chip UC conditions, respectively (Figure S5A, Supporting Information). Considering this, NTA seems to overestimate EV number by taking into account a majority of nonspecific events that would not represent phosphatidylserine-positive vesicles and/or drug-loaded EVs. Therefore, further analyses were performed in order to investigate sample purity.

EV purity of the samples obtained by the different methods was analyzed by NTA and IS^X (Figure 5D,E). We evaluated the NTA purity index that was settled in the literature as the ratio of NTA particle counts to protein concentration: number of particles by NTA/micrograms of proteins by Bradford assay (Figure 5D). Ratios $> 3 \times 10^{10}$ particles μg^{-1} indicate very high EV purity, ratios of 2×10^9 to 2×10^{10} particles μg^{-1} represent low to high purity, and any ratios below 1.5×10^9 particles μg^{-1} evidence impure samples.^[32] For comparison, we tested a new, more restrictive, purity marker based on IS^X data by assuming that only mTHPC positive and AnxV positive events were EVs, relevant as DDS. Sample purity was then evaluated by the number of mTHPC and AnxV double positive events μg^{-1} of proteins by Bradford assay (Figure 5E).

Starvation protocol provided EVs with an NTA purity index of about 2×10^{10} particles μg^{-1} , and the purity was lower for spontaneous release in complete medium and mechanical stress (NTA purity ratios $< 10^{10}$). This trend was similar for purity assessment by IS^X. Hence, although spontaneous release in complete medium provides the highest yield compared to the other production methods, their low purity reveals contaminants of protein aggregate that are copurified from the complete medium.

Purity index could not be calculated in samples isolated by magnetic sorting because the protein concentration was under the detection limit. This suggests that magnetic sorting tends to exclude protein aggregate contaminants that do not comprise iron oxide nanoparticles contrary to EVs. This assumption was supported by IS^X showing higher percentage of AnxV positive events for samples isolated by magnetic sorting compared to ultracentrifugation, regardless of the production protocol (Figure 5A and Figure S5A, Supporting Information).

2.3. Production and Loading Methods Influence EV Size and Cargoes—Confronting Imaging Flow Cytometry and Nanoparticle Tracking Analysis Data

Size distribution by NTA revealed a representative size range of 50–100 nm for EVs spontaneously released in exosome-depleted medium and 100–150 nm for EVs obtained by starvation and mechanical methods (Figure 6A and Figure S5B, Supporting Information), regardless of the isolation method.

Conversely, the most representative size range of double AnxV and mTHPC positive objects by IS^X was 500–1000 nm for EVs spontaneously released in depleted medium and isolated by ultracentrifugation and 100–500 nm for EVs obtained by starvation or mechanical stress method, regardless of the

isolation protocol (Figure 6B). Also, magnetic sorting purified EVs with a larger size range in comparison to ultracentrifugation likely because larger EVs are more responsive to the magnetic field gradient due to a higher magnetic load. The difference between IS^X and NTA size analysis relate to their different detection limit and to the specificity of IS^X to discriminate double mTHPC and AnxV positive objects, thereby limiting analysis mislead due to contamination by protein aggregates.

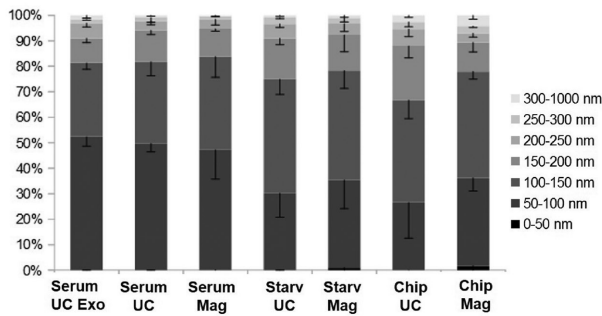
In addition, IS^X allows assessing nanoparticle/drug load distribution in single EVs. Dark field intensity, reflecting nanoparticle load, was higher for EVs isolated by magnetic sorting which selects only the most magnetic EVs (Figure 6C). In contrast, mTHPC fluorescence intensity was higher in EVs produced by starvation and mechanical stress methods when compared to EVs released in complete medium (Figure 6D). Overall, PTS load was also higher for EVs isolated by ultracentrifugation than by magnetic sorting. These results at the single EV level were confirmed by spectrophotometric quantification of the PTS fraction collected in the pellet (Figure S5C, Supporting Information): most of mTHPC was contained in the EV pellet in the case of mechanical stress and starvation-induced EVs, whereas mTHPC was mostly in the supernatant in serum condition.

2.4. Photodynamic Therapeutic Effect of Drug Loaded EVs Is Related to Their PTS Loading

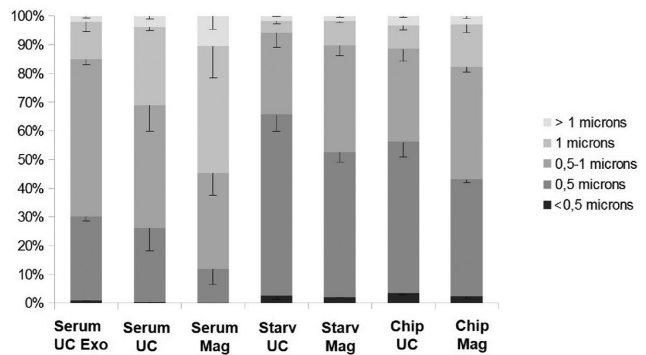
PTS load in EV samples was determined by fluorimetry, indicating 0.5 and 0.7 nanomols of mTHPC in EV samples obtained from one 150 cm² flask via serum UC and starvation UC, respectively. EV samples obtained by starvation and isolated by magnetic sorting as well as EVs produced by the chip method (isolated by UC or magnetic sorting) displayed an mTHPC loading inferior to 0.1 nanomols (Figure 7A).

In vitro cytotoxicity tests were performed on PC3 prostate cancer cells incubated with EVs previous to laser exposure to activate the photosensitizer cargo. Cell metabolic activity decreased to about 10% of the control cell level for EVs produced by serum and starvation conditions and purified by ultracentrifugation, while it was above 70% for all other conditions. Results of mTHPC quantification and EV-induced cytotoxicity were highly correlated. This confirmed that starvation and serum methods produced therapeutic EVs with the highest mTHPC load and that ultracentrifugation was more efficient than magnetic sorting to isolate EV with high PTS content. While IS^X experiments were based on the evaluation of PTS fluorescent properties, this in vitro cytotoxicity test attested that the drug itself remained functional after encapsulation into EVs keeping its therapeutic properties. We also carried out a functional test to evaluate the magnetic field responsiveness of EVs. EVs obtained by the different production methods were inserted in a glass/cover slide chamber featuring a micro-magnet. EVs were found to experience magnetic attraction, being trapped on the magnetic tip. This experiment attested that magnetic nanoparticles conserved their physical properties inside EVs endowing them with magnetic field responsiveness (Figure S6, Supporting Information).

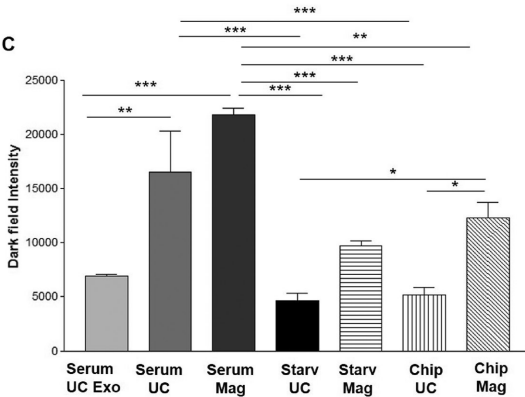
A Size distribution by NTA



B Size distribution by IS^X (AnxV+/mTHPC+ particles)



C



D

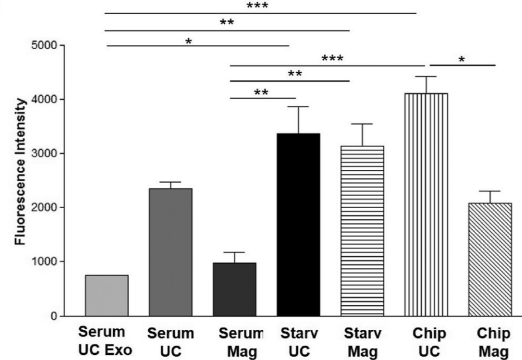
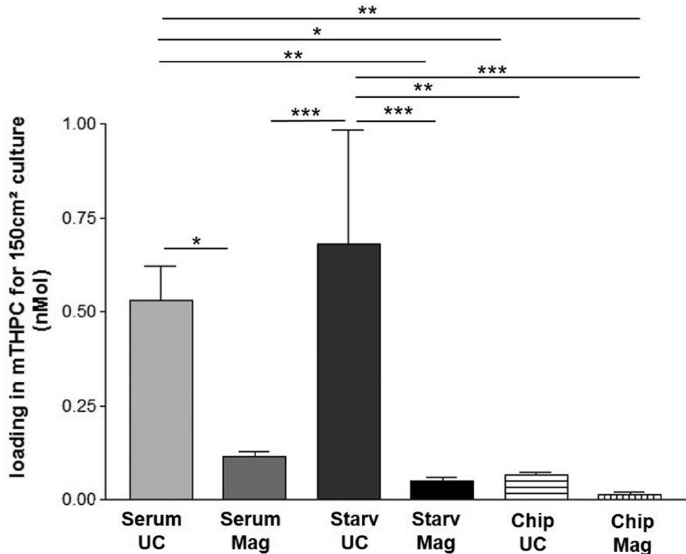


Figure 6. Sizing vesicles by NTA and IS^X. A) Vesicle size distribution by NTA, B) vesicle size distribution of double mTHPC and AnxV positive events by IS^X, C) dark field intensity as indicator of nanoparticle loading for EVs, and D) fluorescence intensity as an indicator of mTHPC loading in each EVs as a function of the production and the purification methods: culture in exosome-depleted complete medium (serum), culture under serum-free starvation (starv), or mechanical stress via the microfluidic chip (chip), purification being performed by ultracentrifugation (UC) or magnetic sorting (Mag). *, **, and *** indicate $P < 0.05$, $P < 0.01$, and $P < 0.001$.

A mTHPC concentration in EVs by fluorimetry



B EV-mediated cytotoxic effect

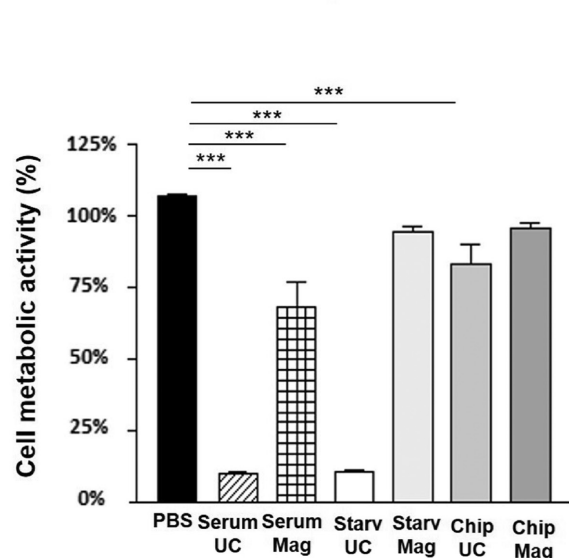


Figure 7. EV loading in photosensitizer (mTHPC) and EV-mediated photocytotoxic effect. A) EV internal loading in PTS corresponding to the total amount of mTHPC in the pellet following ultracentrifugation (100 000 g) as a function of the production and the purification methods: culture in exosome-depleted complete medium (Serum), culture under serum-free starvation (Starv), or mechanical stress via the microfluidic chip (Chip), purification being performed by ultracentrifugation (UC) or magnetic sorting (Mag). B) Cell metabolic activity after treatment with PTS-loaded EVs and irradiation with laser, 100% metabolic activity being the cells not irradiated by the laser. *, **, and *** indicate $P < 0.05$, $P < 0.01$, and $P < 0.001$.

Table 1. Summary table of EVs characteristics.

	Yield		Purity		Loading			Drug delivery
	IS ^X (Anx + / PTS +)	NTA	Particle [μg]	(Anx + / PTS +) [μg]	PM loading/EV	PTS loading/EV	PTS loading (total dose)	Cytotoxicity efficiency
Serum UC	-	+++	-	---	++	++	++	+++
Serum Mag	---	+	Not dosable	Not dosable	+++	+	+	+
Starv UC	+++	++	+++	+++	-	++	+++	+++
Starv Mag	---	---	Not dosable	Not dosable	+	++	-	--
Chip UC	+	--	-	+	+	+++	-	-
Chip Mag	-	---	Not dosable	Not dosable	++	++	--	--

3. Conclusions

Herein, we presented different methods for cellular production and isolation of multifunctional theranostic EVs loaded with inorganic nanoparticles and a drug. Iron oxide nanoparticles and mTHPC photosensitizer were chosen as cargo owing to their respective magnetic and light responsiveness. Apart from remote magnetic manipulation and combined fluorescence and MRI detection, such model EVs display cellular phototoxicity^[25] and heating capability.^[33] Our comprehensive analysis of precursor cells and offspring debris and EVs point out some important differences depending on the production and purification methods. Complementary analyses by NTA and IS^X evidenced that there is a fundamental trade-off between EV nanoparticle load, photosensitizer load, size, yield, purity, and phototoxicity summarized in **Table 1**. Contingent to the targeted application, one could give advantages to EV size, yield, magnetic content, or drug loading and chose the production/isolation methods accordingly.

The presence of copurified protein aggregates misleads yield analysis and size distribution by NTA, especially considering EV produced in complete medium and by mechanical methods. By contrast IS^X analysis of double AnxV and mTHPC events represents a more reliable investigation approach to exclude the interference of such contaminants and specifically detect drug-loaded EVs of interest for theranostic applications. Therefore, we point out a new purity marker based on the ratio of double AnxV and mTHPC positive events by protein mass. This ratio is a more stringent purity marker than the one described in the literature that considers total NTA count events μg⁻¹ of proteins. Based on IS^X purity marker, starvation can be considered the most efficient production method in terms of drug-loaded EV yield, low size, purity, photosensitizer content, and phototoxicity (Table 1). Conversely, EVs spontaneously released in complete medium had a low purity and biased size due to protein contaminants. The mechanical method was clearly the fastest approach as EVs were produced in hours in opposition to days for the other methods, but the yield in therapeutic EVs was low and the method was destructive for cells, producing a high amount of debris or apoptotic bodies. Magnetic sorting purification had the ability to provide the purest samples but the yield was still very low compared to ultracentrifugation. In conclusion, EV production by starvation combined to purification by ultracentrifugation may be considered a reasonable trade-off to provide theranostic EVs on the basis of the patient cells.

Toward the use of EVs as drug delivery vectors, major challenges are still to be overcome. We bet that serum-free methods like starvation are more prone to reach the patient but need to be scaled up to reach human scaled doses.

4. Experimental Section

Cell Culture: HUVECs were cultured as adherent cells at 37 °C and 5% CO₂ in Dulbecco's modified Eagle medium (DMEM) supplemented with 10% fetal bovine serum (FBS) and 100 U mL⁻¹ penicillin and 100 U mL⁻¹ streptomycin.

Magnetic Nanoparticle and Photosensitizer Cell Loading: HUVEC cells were incubated with 8 nm citrate-coated iron oxide nanoparticles (PM, 5 × 10⁻³ M iron in serum-free Roswell Park Memorial Institute (RPMI) medium supplemented with 5 × 10⁻³ M sodium citrate), as previously described,^[34] and/or with the clinically approved photosensitizer (PTS) mTHPC (meta-tetrahydroxyphenylchlorin) or Foscan (10 × 10⁻⁶ M solution in the serum-free RPMI medium) during 2 h at 37 °C.^[25] Incubation was followed by two washing steps in serum-free RPMI medium and a 2 h chase in serum-supplemented DMEM medium in order to allow nanoparticle internalization. Control cells were labeled with PM and PTS 3 d before analysis and kept in complete media.

EV Production in Complete Medium: In order to produce EVs from cells cultured in complete medium containing FBS, the serum was first ultracentrifuged at 100 000 g for 18 h to remove naturally present microvesicles and exosomes. HUVECs were cultured during 3 d with such complete medium containing EV-depleted serum before collecting the conditioned medium for further isolation of the released EVs.

EV Production by Starvation Method: To trigger EV release, cells were cultured in serum-free DMEM for 3 days before collecting the conditioned medium. Serum depletion induced cell stress and the subsequent release of EVs.

EV Production by Mechanical Stress in a Chip: A microfluidic device was designed in order to apply mechanical stress on cells, mimicking blood shear stress on endothelial cells. A master wafer was microfabricated by standard soft lithography techniques. Channels were fabricated featuring a constant length of 500 μm and a width of 5 μm and with a thickness of 10 μm. A microfluidic chip displaying 200 parallel microchannels was produced by casting polydimethylsiloxane (Sylgard 184 kit; Dow Corning) on the master wafer and curing it at 65 °C overnight. The chip was peeled off and bonded to a glass coverslip after plasma activation. When the HUVEC cells were at 90% of confluence, they were detached with cell dissociation buffer (Thermo-Fischer), suspended at 1 × 10⁶ cells mL⁻¹ in the same buffer and transferred to a 10 mL disposable syringe. Cells were then extruded at 4 °C through the fabricated microchannels using a syringe pump at 2 mL h⁻¹. During extrusion, the syringe pump was placed on a shaker to prevent cells from settling. The extrusion medium was recovered.

EV Isolation by Ultracentrifugation: First cell debris were eliminated from conditioned or extrusion medium by 2000 g centrifugation for 10 min. From the supernatant, MVs were isolated after the 10 000 g ultracentrifugation step for 20 min and exosomes (Exo) were further

isolated after the final 100 000 g step (1 h). Alternatively, the total population of EVs (MV + Exo) was isolated with a simple 100 000 g step for 1 h without 10 000 g step. Vesicles were then resuspended in phosphate-buffered saline (PBS). The total amount of proteins recovered was measured by Mini-Bradford assay (Bio-Rad).

EV Purification by Magnetic Sorting: Magnetic sorting was performed on conditioned or extrusion medium after a first centrifugation step for eliminating apoptotic bodies and dead cells (2000 g for 10 min). The medium was transferred to a 10 mL syringe and placed overnight on the edge of a magnet that creates a magnetic field of $B = 650 \text{ mT}$ and a magnetic field gradient $\text{grad}B = 55 \text{ T m}^{-1}$ in the volume of the syringe. The medium was discarded in a sterile hood after removing the nozzle. The EV fraction, which remained on the syringe wall closer to the magnet, was recovered.

Imaging Flow Cytometry of Cells and EVs: The impact of magnetic and/or PTS labeling as well as the impact of EV production method on cell viability, circularity, and cell area was investigated by imaging flow cytometry analysis using an annexin V FITC/propidium iodide (PI) assay kit (Annexin-V-Fluos kit, Roche) according to the manufacturer's instructions. Cell images were acquired using the ImageStream^X (IS^X) multispectral imaging flow cytometer (Amnis Corporation, Seattle), collecting about 10 000 events per sample at 40× magnification. The excitation/emission wavelengths were 488 nm/[470–560] nm for FITC and 561 nm/[595–660] nm for PI. Cells and debris were analyzed by IS^X immediately after labeling with AnxV/PI. AnxV+/PI+ double positive cells were considered as late apoptotic, AnxV+/PI− as early apoptotic, AnxV−/PI+ as necrotic, and AnxV−/PI− double negative as viable. In order to evaluate PTS loading into cells and debris, a 405 nm wavelength laser was used for excitation while the fluorescence images were collected at 660–745 nm spectral detection channel. Dark field images were acquired using a 785 nm laser. Single stained controls were used for compensating fluorescence between channel images on a pixel-by-pixel basis. Cell area and cell circularity was investigated from the bright field picture of each cell, and calculated using a mask and feature from IDEAS image-analysis software (Amnis, Seattle). EV images were also acquired with the IS^X. About 10 000 events per sample were collected at 60× magnification. The presence of PTS and annexin V FITC was investigated in EV samples, using the same excitation/emission wavelength settings as for precursor cells. Nonfluorescent speed beads (calibration SpeedBeads, Amnis, Seattle) of 1 μm were continuously run through the flow during the operation of the IS^X. Speedbeads and Multifluo 0.5 μm beads (Molecular Probes/Invitrogen) were used for size measurement performed on bright field images. Images were analyzed using IDEAS software.

PTS Quantification: The presence of the photosensitizer mTHPC into EVs was estimated by fluorescence spectrophotometry (Cary Eclipse, Varian). Fluorescence emission data at the excitation wavelength of 405 nm were used for obtaining mTHPC spectra. Triton X-100 was used in order to lysate EVs at 0.3% final concentration. Quantification was carried out by means of a calibration curve.

In Vitro Photodynamic Therapy: Human prostate adenocarcinoma PC3 cells were seeded in 24-well plates and incubated overnight at 37 °C in a humidified 5% CO₂ atmosphere. After PBS rinsing, wells were incubated overnight in the dark at 37 °C in a humidified 5% CO₂ atmosphere with 300 μL of EVs in DMEM media without phenol red obtained from around 400 000 cells treated by the different EV production methods. Wells were irradiated individually at a light fluence of 10 J cm^{−2} (100 mW cm^{−2} for 100 s) by means of a 650 nm diode laser featuring a fiber delivery system (BWT, Beijing, China). Cells were incubated for 24 h before cytotoxicity assessment by Alamar Blue test (Invitrogen), according to supplier's instructions. Cells were incubated with 10% Alamar Blue in complete medium for 2 h. After incubation, the medium was transferred to a 96-well plate for analysis using a FLUOstar Optima (BMG Labtech, GmbH) microplate reader (excitation 550 nm, emission 590 nm).

Nanoparticle Tracking Analysis: EV size distribution and concentration were determined with NTA using a Nanosight LM10-HS (NanoSight, UK) with a 532 nm laser. Before measurements, EVs were diluted with sterile PBS (confirmed to be particle free). For each sample, ten movies

of 12 s were recorded using camera level 16 and analyzed by NTA software using the same threshold. NTA postacquisition settings were optimized and kept constant between triplicate analysis.

Micromagnetophoresis: The magnetophoretic velocity of EVs moving toward a micromagnet tip was analyzed using a previously published experimental setup.^[35] In brief, magnetophoresis was observed with a 60× objective from an optical microscope (DMIRB Leica; Leica Microsystems, Wetzlar, Germany) connected to a charge-coupled device camera and a computer. Image J software was used to follow the x,y-position of each individual nanocontainer through the stack of successive frames captured at regular time intervals in a region 100 μm apart from the tip surface (in which the corresponding magnetic field gradient is $\text{grad}B = 194 \text{ T m}^{-1}$).

Statistical Data Analysis: Statistics Data are presented as standard deviation from the mean ($n \geq 3$). Student *t*-test and analysis of variance (ANOVA) test were carried out to determine a significant difference between two or more groups using Prism 3.0 version of GraphPad software (USA). A minimum of 95% confidence level was considered significant (*** indicates $P < 0.0001$; ** indicates $P < 0.01$; * indicates $P < 0.05$, and NS means not statistically significant).

Supporting Information

Supporting Information is available from the Wiley Online Library or from the author.

Acknowledgements

The work was supported by the CardioNanoStem project (IDEX Université Sorbonne Paris Cité) and "Institut de Recherches Internationales SERVIER," and Centre National de la Recherche Scientifique (CNRS). The authors thank Dr. Stephanie Descroix and Dr. Jean-louis Viovy for precious help designing microfluidic chip and Nicole Bogetto at the Plateforme ImagoSeine, Institut Jacques Monod for flow cytometry analysis.

Conflict of Interest

The authors declare no conflict of interest.

Keywords

drug delivery systems, extracellular vesicles, imaging flow cytometry, magnetic nanoparticles, microfluidics, photodynamic therapy

Received: February 23, 2017

Published online:

- [1] S. Wilhelm, A. J. Tavares, Q. Dai, S. Ohta, J. Audet, H. F. Dvorak, W. C. Chan, *Nat. Rev. Mater.* **2016**, *1*, 16014.
- [2] a) S. Kang, S. H. Bhang, S. Hwang, J.-K. Yoon, J. Song, H.-K. Jang, S. Kim, B.-S. Kim, *ACS Nano* **2015**, *9*, 9678; b) M.-R. Choi, R. Bardhan, K. J. Stanton-Maxey, S. Badve, H. Nakshatri, K. M. Stantz, N. Cao, N. J. Halas, S. E. Clare, *Cancer Nanotechnol.* **2012**, *3*, 47.
- [3] M. R. Loebinger, P. G. Kyrtatos, M. Turmaine, A. N. Price, Q. Pankhurst, M. F. Lythgoe, S. M. Janes, *Cancer Res.* **2009**, *69*, 8862.
- [4] a) N. E. Toledano Furman, Y. Lupu-Haber, T. Bronshtein, L. Kaneti, N. Letko, E. Weinstein, L. Baruch, M. Machluf, *Nano Lett.* **2013**, *13*, 3248; b) L. Kaneti, T. Bronshtein, N. Malkah Dayan, I. Kovregina, N. Letko Khait, Y. Lupu-Haber, M. Fliman, B. W. Schoen, G. Kaneti, M. Machluf, *Nano Lett.* **2016**, *16*, 1574.

- [5] a) H. Cao, Z. Dan, X. He, Z. Zhang, H. Yu, Q. Yin, Y. Li, *ACS Nano* **2016**, *10*, 7738; b) J. Fu, D. Wang, D. Mei, H. Zhang, Z. Wang, B. He, W. Dai, H. Zhang, X. Wang, Q. Zhang, *J. Controlled Release* **2015**, *204*, 11.
- [6] a) J. Ratajczak, M. Wysoczynski, F. Hayek, A. Janowska-Wieczorek, M. Ratajczak, *Leukemia* **2006**, *20*, 1487; b) B. Hugel, M. C. Martínez, C. Kunzelmann, J.-M. Freyssinet, *Physiology* **2005**, *20*, 22; c) G. Camussi, M. C. Deregibus, S. Bruno, V. Cantaluppi, L. Biancone, *Kidney Int.* **2010**, *78*, 838.
- [7] a) S. F. Mause, C. Weber, *Circ. Res.* **2010**, *107*, 1047; b) J. J. Jimenez, W. Jy, L. M. Mauro, C. Soderland, L. L. Horstman, Y. S. Ahn, *Thromb. Res.* **2003**, *109*, 175.
- [8] a) M. C. Boelens, T. J. Wu, B. Y. Nabet, B. Xu, Y. Qiu, T. Yoon, D. J. Azzam, C. Twyman-Saint Victor, B. Z. Wiemann, H. Ishwaran, *Cell* **2014**, *159*, 499; b) L. Camacho, P. Guerrero, D. Marchetti, *PLoS One* **2013**, *8*, e73790.
- [9] A. P. Owens, N. Mackman, *Circ. Res.* **2011**, *108*, 1284.
- [10] N. Cloutier, S. Tan, L. H. Boudreau, C. Cramb, R. Subbaiah, L. Lahey, A. Albert, R. Shnyder, R. Gobeze, P. A. Nigrovic, *EMBO Mol. Med.* **2013**, *5*, 235.
- [11] B. S. Holder, C. L. Tower, C. J. Jones, J. D. Aplin, V. M. Abrahams, *Biol. Reprod.* **2012**, *86*, 103.
- [12] P. S. Prakash, C. C. Caldwell, A. B. Lentsch, T. A. Pritts, B. R. Robinson, *J. Trauma Acute Care Surg.* **2012**, *73*, 401.
- [13] a) K. Al-Nedawi, B. Meehan, J. Micallef, V. Lhotak, L. May, A. Guha, J. Rak, *Nat. Cell Biol.* **2008**, *10*, 619; b) R. Valenti, V. Huber, M. Iero, P. Filipazzi, G. Parmiani, L. Rivoltini, *Cancer Res.* **2007**, *67*, 2912.
- [14] P. Vader, E. A. Mol, G. Pasterkamp, R. M. Schiffelers, *Adv. Drug Delivery Rev.* **2016**, *106*, 148.
- [15] P. Kharaziha, S. Ceder, Q. Li, T. Panaretakis, *Biochim. Biophys. Acta* **2012**, *1826*, 103.
- [16] a) R. van der Meel, M. H. A. M. Fens, P. Vader, W. W. van Solinge, O. Eniola-Adefeso, R. M. Schiffelers, *J. Controlled Release* **2014**, *195*, 72; b) S. A. A. Kooijmans, S. Stremersch, K. Braeckmans, S. C. de Smedt, A. Hendrix, M. J. A. Wood, R. M. Schiffelers, K. Raemdonck, P. Vader, *J. Controlled Release* **2013**, *172*, 229.
- [17] R. W. Y. Yeo, R. C. Lai, B. Zhang, S. S. Tan, Y. Yin, B. J. Teh, S. K. Lim, *Adv. Drug Delivery Rev.* **2013**, *65*, 336.
- [18] a) M. Machluf, T. Bronshtein, US Patent US20120164214 A1, **2010**; b) N. E. Toledano Furman, Y. Lupu-Haber, T. Bronshtein, L. Kaneti, N. Letko, E. Weinstein, L. Baruch, M. Machluf, *Nano Lett.* **2013**, *13*, 3248.
- [19] W. Jo, D. Jeong, J. Kim, S. Cho, S. C. Jang, C. Han, J. Y. Kang, Y. S. Cho, J. Park, *Lab Chip* **2014**, *14*, 1261.
- [20] S. C. Jang, O. Y. Kim, C. M. Yoon, D.-S. Choi, T.-Y. Roh, J. Park, J. Nilsson, J. Lötvall, Y.-K. Kim, Y. S. Cho, *ACS Nano* **2013**, *7*, 7698.
- [21] B. György, K. Módos, É. Pállinger, K. Pálóczi, M. Pásztói, P. Misják, M. A. Deli, Á. Sipos, A. Szalai, I. Voszka, A. Polgár, K. Tóth, M. Csete, G. Nagy, S. Gay, A. Falus, Á. Kittel, E. I. Buzás, *Blood* **2011**, *117*, e39.
- [22] H. G. Lamparski, A. Metha-Damani, J.-Y. Yao, S. Patel, D.-H. Hsu, C. Ruegg, J.-B. Le Pecq, *J. Immunol. Methods* **2002**, *270*, 211.
- [23] a) S. Mathivanan, J. W. Lim, B. J. Tauro, H. Ji, R. L. Moritz, R. J. Simpson, *Mol. Cell. Proteomics* **2010**, *9*, 197; b) B. J. Tauro, D. W. Greening, R. A. Mathias, S. Mathivanan, H. Ji, R. J. Simpson, *Mol. Cell. Proteomics* **2013**, *12*, 587.
- [24] A. N. Böing, E. van der Pol, A. E. Grootemaat, F. A. W. Coumans, A. Sturk, R. Nieuwland, *J. Extracell. Vesicles* **2014**, *3*, 23430.
- [25] A. K. Silva, J. Kolosnjaj-Tabi, S. Bonneau, I. Marangon, N. Boggetto, K. Aubertin, O. Clément, M. F. Bureau, N. Luciani, F. Gazeau, *ACS Nano* **2013**, *7*, 4954.
- [26] Y. Lee, S. EL Andaloussi, M. J. A. Wood, *Hum. Mol. Genet.* **2012**, *21*, R125.
- [27] D. A. Basiji, W. E. Ortyń, L. Liang, V. Venkatachalam, P. Morrissey, *Clin. Lab. Med.* **2007**, *27*, 653.
- [28] I. Marangon, N. Boggetto, C. Ménard-Moyon, E. Venturelli, M.-L. Béoutis, C. Péchoux, N. Luciani, C. Wilhelm, A. Bianco, F. Gazeau, *Nano Lett.* **2012**, *12*, 4830.
- [29] A. Riches, E. Campbell, E. Borger, S. Powis, *Eur. J. Cancer* **2014**, *50*, 1025.
- [30] a) U. Erdbrügger, C. K. Rudy, M. E. Etter, K. A. Dryden, M. Yeager, A. L. Klibanov, J. Lannigan, *Cytometry, Part A* **2014**, *85*, 756; b) S. E. Headland, H. R. Jones, A. S. V. D'Sa, M. Perretti, L. V. Norling, *Sci. Rep.* **2014**, *4*, 5237; c) K. Goda, A. Ayazi, D. R. Gossett, J. Sadasivam, C. K. Lonappan, E. Sollier, A. M. Fard, S. C. Hur, J. Adam, C. Murray, *Proc. Natl. Acad. Sci. USA* **2012**, *109*, 11630.
- [31] R. A. Dragovic, C. Gardiner, A. S. Brooks, D. S. Tannetta, D. J. P. Ferguson, P. Hole, B. Carr, C. W. G. Redman, A. L. Harris, P. J. Dobson, P. Harrison, I. L. Sargent, *Nanomed. Nanotech. Biol. Med.* **2011**, *7*, 780.
- [32] J. Webber, A. Clayton, *J. Extracell. Vesicles* **2013**, *2*, 3402.
- [33] A. K. A. Silva, R. Di Corato, T. Pellegrino, S. Chat, G. Pugliese, N. Luciani, F. Gazeau, C. Wilhelm, *Nanoscale* **2013**, *5*, 11374.
- [34] A. Al Faraj, F. Gazeau, C. Wilhelm, C. Devue, C. L. Guérin, C. Péchoux, V. Paradis, O. Clément, C. M. Boulanger, P.-E. Rautou, *Radiology* **2012**, *263*, 169.
- [35] A. K. A. Silva, R. Di Corato, F. Gazeau, T. Pellegrino, C. Wilhelm, *Nanomedicine* **2012**, *7*, 1713.